9 Surface Physics

T. Greber, M. Hengsberger, J. Wider, M. Hoesch, W. Auwärter, M. Muntwiler, A. Tamai, A. Dolocan, M. Corso, C. Cirelli, T. Gresch, Ch. Schlepütz, M. Klöckner, W. Deichmann, J. Osterwalder

The surface physics laboratory is well equipped for the preparation and characterization of clean surfaces, ultrathin films and nanostructures under ultrahigh vacuum (UHV) conditions. Experimental techniques available to us include x-ray photoelectron spectroscopy (XPS) and diffraction (XPD), angle-resolved photoemission spectroscopy (ARPES), two-photon photoemission (2PPE) using femtosecond laser pulses, low-energy electron diffraction (LEED) and scanning tunneling microscopy (STM). At the nearby Swiss Light Source we have built up two more photoemission spectrometers, one for spin-resolved Fermi surface mapping and one for near-node photoelectron holography.

The research carried out during the report period can be grouped into four topics:

- *Surface states on clean metal surfaces*
  The close-packed (111) surfaces of several face-centred-cubic metals (e.g. Au, Ag, Cu, Ni) exhibit so-called Shockley surface states that propagate almost freely within the surface plane, and which have wave functions that decay exponentially both into the vacuum and into the bulk of the crystal. They thus exemplify a two-dimensional gas of nearly-free electrons (2DEG), which manifests itself in parabolic energy dispersion relations. On Au(111), this 2DEG is subject to spin-dependent momentum shifts due to the Rashba effect. We have measured these momentum shifts and the detailed spin structure in reciprocal space (Section 9.1). On vicinal Cu(111) surfaces we could show that the wavefunction of this 2DEG can localize on individual terraces, while photoemission matrix element effects still make the measured dispersion look free-electron-like (Section 9.2).

- *Monolayer films of hexagonal boron nitride on metal surfaces*
  The preparation of well-defined monolayer-thick films permits us to study the structural, electronic and magnetic properties at an interface between two different materials. In the nanosciences, such knowledge is essential for the understanding of how nanoscale structures and devices function. We have continued to study single monolayers of hexagonal boron nitride (*h*-BN) on transition metal surfaces as well-defined model cases for metal-insulator junctions. A new and more convenient precursor molecule was demonstrated to produce high quality films on Ni(111) (Section 9.3). On Rh(111) the *h*-BN film self-assembles into a remarkable nanostructure in the form of a two-layer nanomesh (Section 9.4), while on Pd(110) a variety of Moiré patterns is found (Section 9.5).

- *Adsorbed molecules*
  Molecular monolayers offer a highly interesting route to prepare functionalized surfaces. Chemists provide molecules with suitable chemical anchors and with the desired functional groups that are to be exposed at the surface. We are working on methods that can measure the bonding geometry of the molecules on the substrate, and we study the electronic properties of molecular layers that have a high degree of self-organized crystalline order within the layer. For C_{60} molecules on Ag(111) we find a strong dependence of the molecular orientation on the degree of potassium doping of the layer (Section 9.6). In Section 9.7 a new and efficient procedure is presented for unraveling the presence of several molecular orientations in such monolayers and quantifying their relative abundances. For a C_{60} layer on *h*-BN/Ni(1 1 1) a new type of phase transition is revealed where the charge transfer to the molecules changes due to a thermally excited rocking motion of the molecules (Section 9.8). In Section 9.9 the adsorption geometry of tartaric acid on Cu(110) is measured by a new generation XPD experiment that makes use of the high-brightness tuneable

synchrotron radiation of the SLS. The XPD patterns display directly the chiral character of the molecule when single enantiomers are adsorbed, as well as the conformation changes due to the interaction with the metal substrate.

- *Time-resolved electron diffraction*
  The setup of our picosecond time-resolved electron diffraction experiment is complete, and we have seen the first temporal correlation signals between laser pump pulses and electron probe pulses. This was achieved by aiming the electrons through a fine pinhole in a metal plate while hitting the entrance of the pinhole with the laser pulses (Section 9.10). The space charge produced by the laser light acts like a time-dependent valve for the electron pulse. This relatively simple setup can now be used in order to establish spatial and temporal overlap of the two pulses on a sample surface.

9.1 The spin-structure of the Shockley surface state on Au(111)

in collaboration with:
V.N. Petrov, St. Petersburg Technical University, Russia and L. Patthey, M. Shi and M. Falub, Swiss Light Source, Paul Scherrer Institut, 5232 Villigen, Switzerland

The reduced symmetry of a two-dimensional electron gas confined by asymmetric boundaries can result in a spin-splitting of the electronic levels in momentum space (Rashba splitting). Such a separation of up- and down-spins in k-space might be useful as a source of polarized electrons in future spintronic devices. The fundamental physics governing the strength and the detailed behaviour of the splitting have been investigated. The (111) surface of gold accommodates a Shockley-type surface state. This two-dimensional quasi-free electron gas is a model case; it displays a strong spin-orbit splitting proportional to the in-plane momentum of the electrons [1; 2; 3].

The spin-resolved photoelectron spectrometer COPHEE installed at the Surface and Interface Spectroscopy (SIS) beamline at the Swiss Light Source was used to investigate in detail the Fermi surface of the surface state on Au(111). For the first time a complete spin-resolved angular mapping of the photoelectrons emitted with linear polarized VUV radiation was performed. Such a mapping allows to determine the individual contributions to the Fermi surface from electrons of opposite spin. For the two-dimensional free-electron gas the Rashba model predicts the spins to lie in the surface plane, with a momentum shift for spins pointing in a counterclockwise (clockwise) direction tangential to the Fermi surface. Therefore we chose the tangential direction as the reference direction for spin-up and spin-down. An out-of-plane component of the spin-polarization is only expected if the electrons interact with the nuclear charge in such a way that an electrical field component parallel to the surface plane is experienced. Figure 9.1 shows the measured momentum distribution pattern of the surface state photoelectrons (a) and the tangential (b) and out-of-plane (c) components of the spin-polarization. The sample was cleaned by repeated sputtering and annealing cycles and held at $\approx$150 K during the measurements. The data were acquired in a 7 hrs. long continuous scan. In the polarization maps the modulation of the polarization components can be studied. From the intensity (a) and the in-plane polarization (b), which is obviously the dominant component, the spin-resolved intensities for spin-up (d) and spin-down (e) were calculated. Note the two individual Fermi surfaces with different radii (Fermi wave vectors). A detailed analysis of the polarization modulations for both the in-plane and the out-of-plane component was performed. Any modulation must reflect the three-fold symmetry of the surface. It was found that the polarization follows the tangent to the circular Fermi surface. No modulation could be observed within the detection limit of 2% (electron polariza-

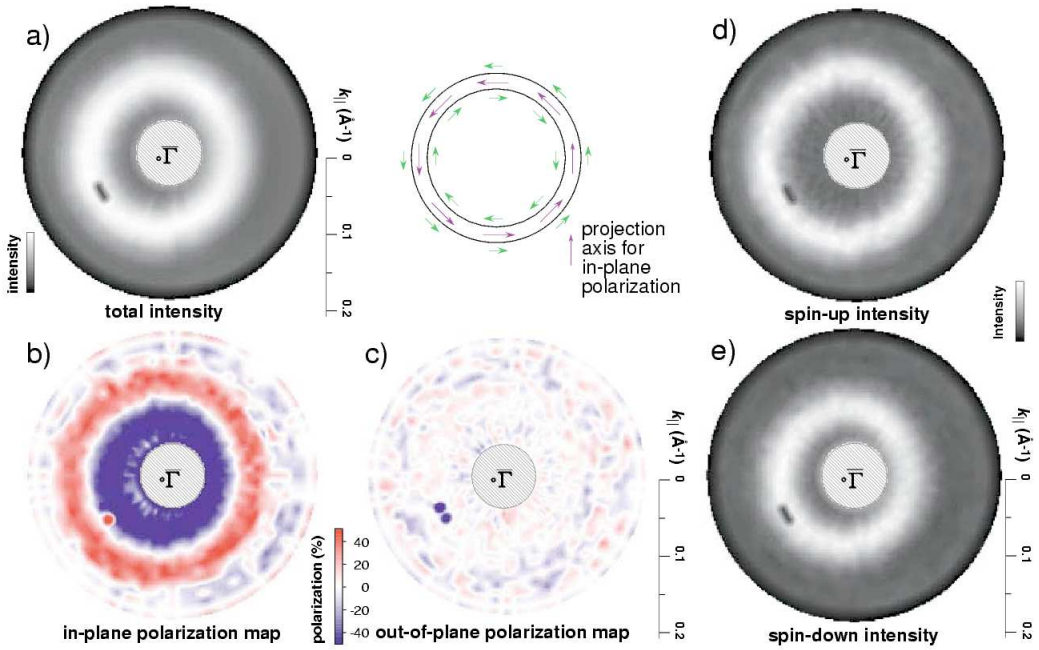

Figure 9.1: *Spin-resolved momentum distribution maps near the Fermi surface (E_B=170 meV) measured with UV-light of $\hbar\omega = 21.1$ eV.*
a) Total intensity map and a sketch of the Fermi surface and the predicted spin structure (guide to the eye). Purple arrows indicate the projection axes for in-plane polarization.
b) and c) Polarization maps in a color-scale representation for the in-plane component (b) and for the out-of-plane component (c) of the polarization vector. The in-plane polarization (b) is a projection on the tangents to the circular Fermi surface. Red (blue) indicates a counter-clockwise (clockwise) spin orientation.
d) and e) Individual spin-up and-spin down intensity maps derived from a) and b).

tion value). This allows the conclusion that the electrons experience on the average an electrical field perpendicular to the surface and the free-electron picture applies very well to the description of the surface state, including its spin structure.

[1] S. LaShell, B.A. MacDougall, E. Jensen, Phys.Rev.Lett.77 (1996) 3419.
[2] G. Nicolay, F. Reinert, S. Hüfner, P. Blaha,Phys.Rev.B 65 (2001) 33407.
[3] M. Muntwiler, M. Hoesch, V. N. Petrov, M. Hengsberger, L. Patthey, M. Shi, M. Falub, T. Greber, and J. Osterwalder, J. Electron Spectrosc. Relat. Phenom. in press (2004).

9.2 Localization of surface states in disordered step lattices

in collaboration with: L. Patthey, M. Shi and J. Krempasky, Swiss Light Source, Paul Scherrer Institut, 5232 Villigen, Switzerland

Real single crystal surfaces contain a variety of more or less complex defects. Isolated monoatomic steps are the most frequent imperfections on clean surfaces. It is known that such defects have a profound influence on many surface-related phenomena, such as heterogeneous catalysis, heteroepitaxy or self assembly of molecular super-structures. However, the underlying changes of the electronic

structure in the presence of defects are still poorly understood. As a model system, we have investigated the electronic structure of several vicinal Cu surfaces that can be obtained by cutting a single crystal under a small angle with respect to the dense (111) planes. Suitably prepared, these surfaces exhibit hexagonally close packed terraces of a few atomic spacings width, bounded by a monoatomic step lattice, where the lattice constant may be chosen by varying the miscut angle. Since the repulsive interactions between steps are comparable with thermal energies, fluctuations in the lattice positions, mediated by diffusion of atoms along the step edges, are unavoidable. Thus, step positions oscillate around their nominal lattice points, analogous to thermal vibrations in an atomic lattice. However, the frequencies of these oscillations are much lower than those of lattice vibrations, and the amplitudes reach values which would cause a single crystal to melt. It is thus natural to ask whether electronic states still propagate under such conditions or whether they tend to localize, as expected for amorphous or liquid condensed matter. This allows to study electronic properties in a unique structural regime, hardly accessible otherwise.

We used the free-electron-like Shockley surface state as an electronic probe of the disordered step–lattice. This state has been shown to remain free-electron like on vicinal Cu(111) surfaces with small step–step separations (< 15Å). In this regime, the step–lattice is well ordered and thus can be treated as a one–dimensional super–lattice which causes a slightly anisotropic dispersion of the surface state, but does not cause localization. Increasing the terrace width to a critical value of half of the surface state Fermi wave length, we recently found the opening of super–lattice band gap, which clearly demonstrates that a description of the step arrays as super–lattice is appropriate [1]. On the other hand, recent experiments of Mugarza *et al.* revealed that surface states on vicinal Au(111) fully localize perpendicular to the step direction for terrace widths > 30Å, while they remain free-electron-like along the steps [2]. This result was in contrast to earlier experiments on vicinal Cu, which always showed free-electron-like dispersing states, also for terrace lengths where a super–lattice description is inappropriate. Analyzing our recent experiments carried out at the SIS beamline of the Swiss Light Source, we could show that the roughly parabolic band of high intensity observed previously in photoemission from vicinal Cu is not indicative of propagating states, but is fully consistent with the assumption of lateral quantum well states localized on single terraces [3]. This is illustrated in Fig. 9.2, where we simulated photoemission This is illustrated in Fig. 9.2, where we simulated photoemission

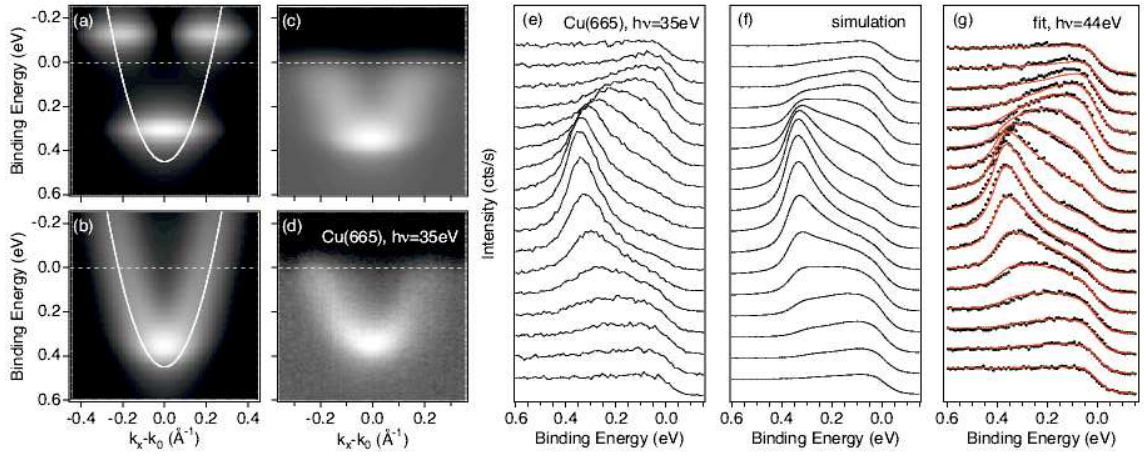

Figure 9.2: *Simulation of photoemission data from the Shockley surface state on Cu(665). a) Intensity distribution for isolated quantum wells of 25Å width, assuming a line width of 90meV. b) same for a Gaussian distribution of the well–width. c) Simulated intensity distribution from (b) with a constant background and multiplied with a Fermi function. d) Photoemission data from Cu(665). e),f) EDCs from c) and d). g) Fit to a refined model (for details see Ref. [3]).*

data expected from single decoupled lateral quantum wells, and from a distribution of quantum wells with different widths, as found on vicinal surfaces with large step–step separations. The apparently parabolic band, which closely resembles the experimental data, arises as a consequence of the strong momentum dependence of the matrix element in conjunction with the averaging over different terrace sizes.

[1] F. Baumberger, M. Hengsberger, M. Muntwiler, M. Shi, J. Krempasky, L. Patthey, J. Osterwalder, and T. Greber, Phys.Rev.Lett.**92**, 016803 (2004).

[2] A. Mugarza, A. Mascaraque, V. Pérez–Dieste, V. Repain, S. Rousset, F.J. García de Abajo, and J.E. Ortega, Phys.Rev.Lett.**87**, 107601 (2001).

[3] F. Baumberger, M. Hengsberger, M. Muntwiler, M. Shi, J. Krempasky, L. Patthey, J. Osterwalder, T. Greber, Phys.Rev.Lett., in press.

9.3 Synthesis of one monolayer of hexagonal boron nitride on Ni(111) from B-trichloroborazine $(ClBNH)_3$

in collaboration with: H.U. Suter, Physik Institut der Universität Zürich, and H. Sachdev, Institut f. Anorg. Chemie, Universität des Saarlandes, D-66041 Saarbrücken, Germany

Single layer h-BN films may be grown on Ni(111) by using B-trichloroborazine $(ClBNH)_3$ as a molecular precursor [1]. This way of producing stoichiometric, ultimately thin h-BN layers is an alternate route to the use of borazine $(HBNH)_3$ [2; 3]. The handling of borazine, a reactive liquid, is not very simple, whereas B-trichloroborazine sublimates from the solid phase. The decomposition reaction of the molecules to form the h-BN film proceeds at 1000 K via the path $(ClBNH)_3$ + Ni(111) $\rightarrow$ h-BN/Ni(111) + 3(HCl). Scanning tunneling microscopy (STM) experiments show that high quality films can be grown, as for the more established method that uses borazine [4] (see Fig. 9.3). The h-BN growth patterns indicate a reaction mechanism proceeding via ring opening of these cyclic BN molecules. A set of density functional calculations for B-trichloroborazine, borazine and N-trichloroborazine yields bond energies and bond lengths in these molecules and helps rationalizing the similar film morphologies and defects irrespective of the use of $(HBNH)_3$ [4] or $(ClBNH)_3$ [1].

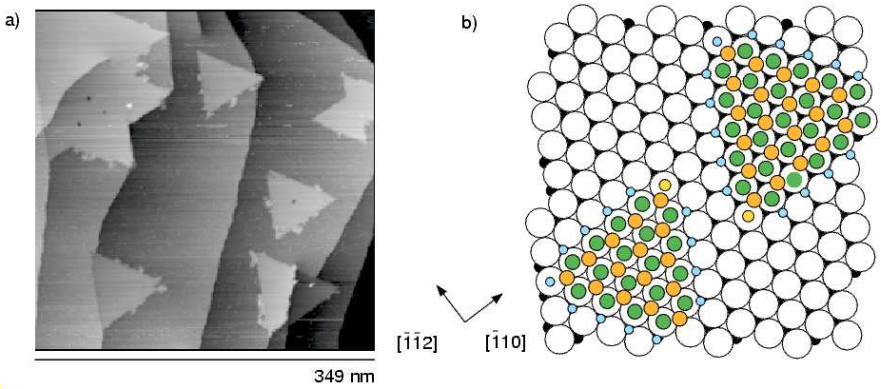

Figure 9.3: *Single layer h-BN islands on Ni(111). a) STM image from a partial coverage of h-BN on Ni(111) as formed from B-trichloroborazine (V_{sample}=-0.2V, I_t=0.5nA). The triangles with opposite orientations are h-BN islands with B on fcc and B on hcp sites, respectively. b) Corresponding hard sphere models for the two types of islands with hcp (left) and fcc (right) domains. From [1].*

[1] W. Auwärter, H.U. Suter, H. Sachdev and T. Greber, Chem. Mater. **16**, 343 (2004).
[2] A. Nagashima, N. Tejima, Y. Gamou, T. Kawai, and C. Oshima, Phys.Rev.B **51**, 4606 (1995).
[3] W. Auwärter, T.J. Kreutz, T. Greber, J. Osterwalder, Surf. Sci. **429**, 229 (1999).
[4] W. Auwärter, M. Muntwiler, J. Osterwalder and T. Greber, Surf. Sci. **545**, L735 (2003).

9.4 Boron nitride nanomesh

A new mesh-like nanostructure (Fig. 9.4a) is found when *h*–BN is deposited on the Rh(111) surface [1]. The large lattice mismatch of 6.7% between the two systems is likely the main reason leading to its formation. Due to its highly regular periodicity of 3 nm it is a unique link between the nano- and mesoscopic world, so that it can be easily used as a template to organize molecules into supramolecular structures. It is thermally stable up to 1000 K and resistant to air exposure.

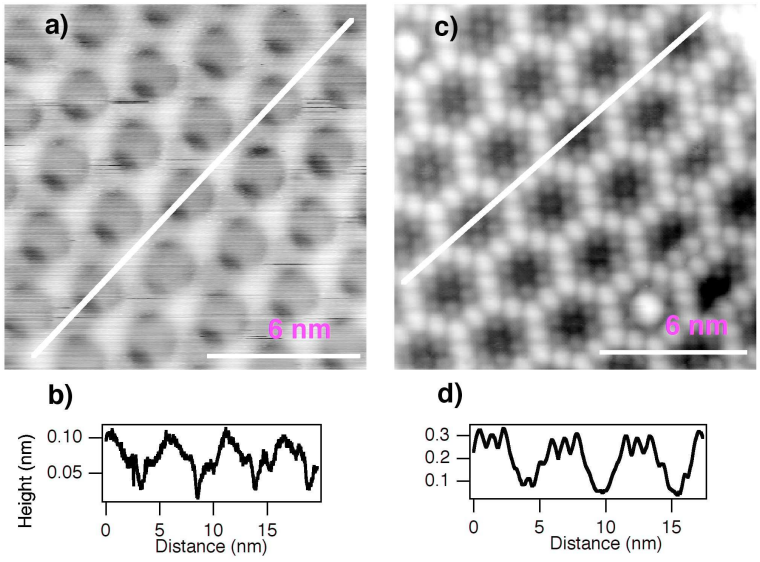

Figure 9.4:
a) Constant–current STM image (-2 V and 1.0 nA) of the h–BN nanomesh.
b) Cross–sectional profile along the white line in a).
c) Constant–current STM image (-2 V and 1.5 nA) of roughly one monolayer of C_{60} adsorbed on the nanomesh.
d) Cross–sectional profile along the white line in (c).

This structure self-assembles when the clean Rh(111) surface is kept at 1070 K during exposure to 40 L of borazine $(HBNH)_3$. From the calibration with x–ray photoelectron spectroscopy of the B1s and N1s signals with respect to Rh3s, a coverage of 1.5 ML of *h*–BN on Rh(111) is calculated. The analysis of STM images combined with LEED pattern information results in the following picture: the hexagonal nanomesh consists of two atomic mesh layers with a periodicity of 32 ± 2 Å which corresponds to 13×13 *h*–BN unit cells growing on top of 12×12 Rh unit cells. The hole diameter of the top layer is 24 ± 2 Å; it may be slightly smaller in the bottom one. The mesh wire width is 9 ± 2 Å. The two layers are offset in order to cover most of the metal surface. While the first layer sits flat on the substrate, the second one behaves like a corrugated sheet which follows the underlying topography: it is pulled into the first layer holes and pushed out when superimposed on the first layer wires. The real height of the nanomesh cannot be directly extracted from STM images such as the one in Fig. 9.4a. The line profile in Fig. 9.4b indicates that the step height from the Rh surface to the first *h*–BN layer as well as from the first to the second layer is only 0.5 Å. This is due to electronic effects, since the *h*–BN layer is an insulator (in the sense that there are no *h*–BN electronic states in the Rh–d band region and at the Fermi level), and the STM images thus reflect the lateral changes of the tunneling resistance through the nanomesh. The real corrugation can be observed when C_{60} molecules are deposited on the structure (Fig. 9.4c). They decorate the mesh and 11 to 13 molecules are found in each unit cell. The corrugation of the layer is here 2 Å (Fig. 9.4d), indicating *h*–BN step heights as on Ni(111) [2].

[1] M. Corso, W. Auwärter, M. Muntwiler, A. Tamai, T. Greber, J. Osterwalder, Science **303** (2004) 217.

[2] M. Muntwiler, W. Auwärter, F. Baumberger, M. Hoesch, T. Greber, J. Osterwalder, Surf. Sci. **472** (2001) 125.

9.5 *h*–BN/Pd(110): a hexagonal covalent network on a rectangular substrate

The properties of hexagonal boron nitride monolayers adsorbed on the Ni(111) surface have been studied for several years, because this system represents a model case for a perfect metal/insulator junction [1]. Due to the small compressive lattice mismatch of 0.4%, the *h*–BN forms large ordered terraces with a low corrugation of 0.1 Å. In the case of *h*–BN/Rh(111), the large tensile lattice mismatch of 6.7% between the two systems leads to the formation of the bilayer nanomesh discussed in the previous section. What happens when the *h*–BN unit cells aggregate on a non-hexagonal and incommesurate substrate?

On the Pd(110), the *h*–BN units do not find a unique way to register with the substrate. As a consequence, they form many different domains of Moiré patterns distributed randomly over the surface.

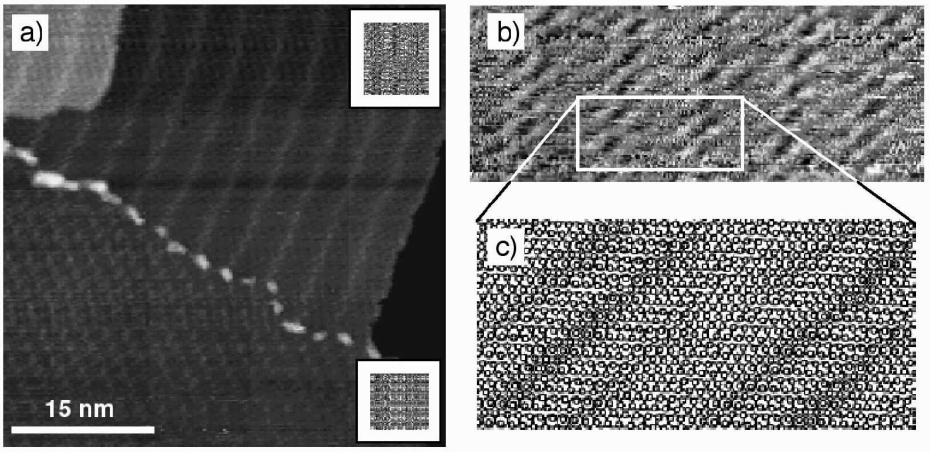

Figure 9.5:
a) Constant–current STM image (1.0 V and 1.0 nA) of h–BN/Pd(110) showing two different Moiré patterns separated by a domain boundary. The inset in the top right corner depicts an atomic model for the upper Moiré domain (see (b) and (c)), the one in the bottom right corner is an atomic model for the lower domain.
b) High resolution STM image for a region of the upper domain.
c) Atomic model for this same domain, where a layer of boron nitride, represented by nitrogen atoms only, is placed on the substrate, rotated clockwise by 5 degrees with respect to [001] crystallographic direction of the Pd(110) surface. In b) it can be seen that the STM images bright ridges along the darker Moiré stripes, leading to the continuous bright stripes in a) for this domain. This is believed to be due to an electronic effect.

The LEED patterns recorded over a wide energy range (from 50 to 300 eV) show that each palladium principal lattice spot is surrounded by a large circle. This indicates that the *h*–BN domains are oriented randomly with respect to the substrate surface. The radii of the circles correspond to the lattice constant of *h*–BN. The Moiré domains show clearly in STM images from monolayer films (Fig. 9.5a).

They are separated by domain boundaries that are decorated by white features of an apparent height of 1.8 ± 0.3 Å. The Moiré contrast can be understood with a simple atomic model placing a *h*–BN layer, represented by the nitrogen atoms alone, on top of the Pd(110) surface layer. By varying the azimuthal orientation between film and substrate, various domain patterns similar to those observed in STM images can be generated. This procedure is justified since it has recently been found that, under similar tunneling conditions, it is primarily the N atoms that are imaged by the STM [2]. Figure 9.5b shows a close-up STM image of the upper domain, with its characteristic Moiré stripes that are well reproduced by the model depicted in Fig. 9.5c.

[1] W. Auwärter, One Monolayer of Hexagonal Boron Nitride on Ni(111): an Atomically Sharp Interface, PhD thesis Universität Zürich (2003).

[2] G. B. Grad, P. Blaha, K. Schwarz, W. Auwärter, T. Greber,Phys.Rev.B **68** (2003) 085404.

9.6 Doping induced reorientation of C_{60} molecules on Ag(111)

in collaboration with:
Z.-X. Shen, Physik-Institut, Universität Zürich (while on Sabbatical) and Department of Applied Physics and Stanford Synchrotron Radiation Laboratory, Stanford University, Stanford, USA

Alkali–doped C_{60} compounds (fullerides) present a lot of interesting properties. Depending on the concentration of the dopant they display metallic or insulating behaviour, and they even become superconducting at temperatures as high as the best conventional superconductors. The variety of different electronic properties observed has been assigned to the simultaneous importance of electron-phonon and electron-electron interactions [1].

Only recently it became possible to measure the band dispersion of the partially filled lowest unoccupied molecular orbital (LUMO) in the electron doped C_{60}/K/Ag(111) system [2]. Density functional calculations (DFT) indicate that the electronic band dispersion is highly sensitive to the relative ori-

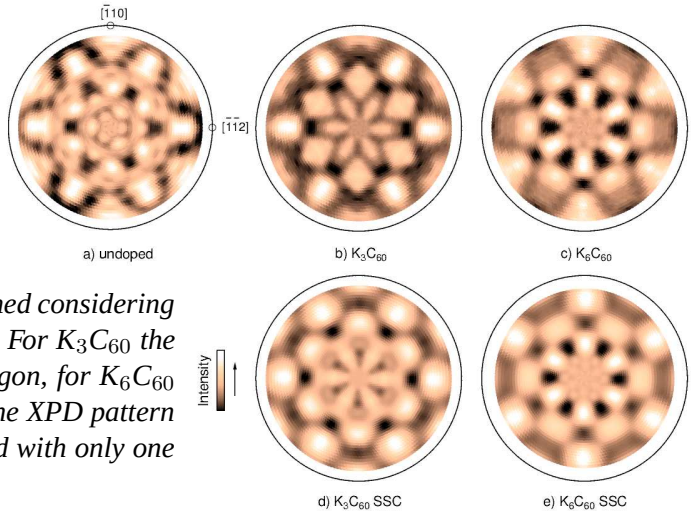

Figure 9.6:
C 1s XPD patterns from one monolayer of C_{60} on the Ag(111) surface.
a), b) and c) Experimental patterns for one undoped monolayer, K_3C_{60} and K_6C_{60}, respectively.
d) and e) Calculated SSC patterns obtained considering one inequivalent molecular orientation: For K_3C_{60} the molecule face the surface with the hexagon, for K_6C_{60} with the bond between two hexagons. The XPD pattern from the undoped layer cannot be solved with only one orientation of the molecule.

entation of neighboring molecules [2]. In order to determine experimentally the orientation of the C_{60} molecules on Ag(111) and to investigate the role of potassium as a dopant we used angle–scanned x–ray photoelectron diffraction (XPD). This technique has already shown to be a very powerful tool for measuring the orientation of C_{60} adsorbed on different metallic surfaces [3].

In Figs. 9.6a), b) and c) we show the experimental patterns for three doping levels. The pronounced differences reveal that potassium induces a change in the orientation of the molecule. In the undoped monolayer the experimental pattern corresponds to more than one defined orientation. Upon doping with potassium the layer gets ordered and two different orientations can be identified for K_3C_{60} and K_6C_{60}. The single–scattering cluster (SSC) calculations were obtained considering one orientation (Figs. 9.6d) and e)). They reproduce quite well the overall positions and shapes of the prominent forward-focusing maxima in the experimental patterns. When the LUMO is half-filled (K_3C_{60}) the molecules face the surface with a hexagon. When the LUMO is fully occupied (K_6C_{60}) they face it with a bond between two hexagons. An azimuthal rotation of the molecule away from the high symmetry crystal axes of the substrate is found for both doping levels. The orientation found in this analysis for K_3C_{60} is in reasonable agreement with that expected from the DFT calculations [2]. K2*p* XPD reveals the same change in the orientation of the molecules and gives indications for the dopant sites in both cases. The reorientation of C_{60} induced by potassium is important to understand the effects of doping on the electronic properties of fullerides.

[1] O. Gunnarsson, Rev. Mod. Phys. **69** (1997) 575.

[2] W.L. Yang et al., Science **300** (2003) 303.

[3] R. Fasel, P. Aebi, R.G. Agostino, D. Naumovic, J. Osterwalder, A. Santaniello, L. Schlapbach, Phys.Rev.Lett.**76** (1996) 4733.

9.7 Automated determination of coexisting inequivalent orientations of C_{60} molecules on Ag(111)

As is exemplified in the previous section, XPD has great potential for determining the orientation of large adsorbed molecules on metallic surfaces, especially in the case of C_{60}. Experimental XPD patterns are usually compared with simulated ones produced by single–scattering cluster (SSC) calculations. Using a vast trial–and–error structure search, it has even been possible to determine the relative abundance of two coexisting orientations of C_{60} on a Ag(001) surface [1]. Attempts to fit the pattern recorded from C_{60} molecules adsorbed on a Ag(111) surface (see Fig. 9.6a), however, provided no satisfactory conclusion concerning the molecular orientations. One plausible cause might be the limitation of the maximum number of coexisting inequivalent orientations in the available fitting routines.

The scope of this work has been to approach in a more general way the problem of fitting XPD patterns to a combination of simulated orientations. One would like to specify any arbitrary maximum number of coexisting orientations for the fit. The routine should be kept as material-unspecific as possible, thus allowing analysis of different molecular adsorbate systems. As in earlier procedures, the multipole expansion of the experimental pattern is compared with a linear combination of a limited set of calculated patterns representing inequivalent orientations. New features include minimization of a reliability factor via simulated annealing techniques, the rotation of the simulated patterns directly in the space of their multipole expansion coefficients, and automatic determination of the relative abundance of the present orientation through freely variable weight factors.

First tests have shown that the routine reliably reproduces arbitrary linear combinations of simulated patterns. The abundances of up to five different orientations with weight factors ranging from 0.04 to 0.45 have been correctly identified to within 0.1 percent of the total composition (see Fig. 9.7). The application to real experimental data has been hindered so far by issues concerning the intrinsic background of the measurements. A possible normalization procedure to counter this problem has been implemented, but is not yet fully operational.

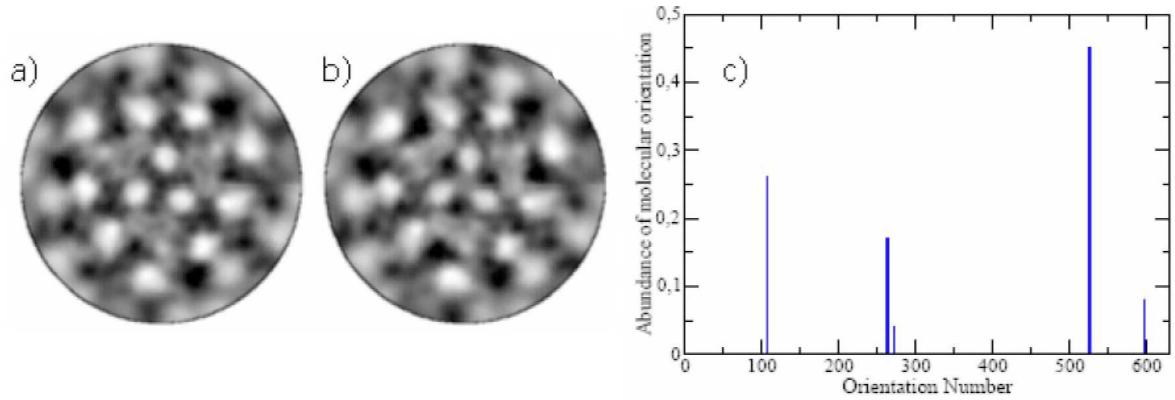

Figure 9.7: *First fitting results:*
a) simulated test pattern for C 1s emission from C_{60} molecules, representing the linear combination of 5 arbitrary inequivalent orientations,
b) the fit result for that test pattern and
c) the histogram showing the fitted orientation distribution.
For all but the correctly identified 5 orientations from the test pattern the weight factors are < 0.0002. The abundances of the five present orientations have been correctly identified to within 0.1% of the total composition.

[1] C. Cepek, R. Fasel, M. Sancrotti, T. Greber, J. Osterwalder, Phys.Rev.B **63** (2000) 125406.

9.8 Temperature-dependent charging of monolayer C_{60} on *h*-BN/Ni(1 1 1)

in collaboration with: A. Seitsonen, Physikalisch-Chemisches Institut der Universität Zürich

Monolayer hexagonal boron nitride (*h*-BN) on Ni(1 1 1) represents an atomically sharp insulating layer with well-known structure (see also Section 9.3) on a ferromagnetic substrate. With a metallic adsorbate deposited on top of it, it could form a model metal-insulator-metal interface for developing and testing charge and spin transport theory across magnetic heterojunctions. In contrast to elemental metals that either form three-dimensional clusters on top of *h*-BN or intercalate underneath, C_{60} forms a compact wetting layer on *h*-BN/Ni(1 1 1) [1]. C_{60} layers become metallic upon doping with alkali metals [2], and a C_{60}/*h*-BN/Ni(1 1 1) layer structure may thus represent such a model system.

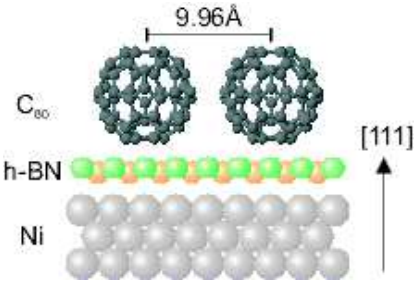

Figure 9.8:
Model of the adsorption geometry of monolayer C_{60} on h-BN/Ni(1 1 1) (side view).
The molecules arrange themselves in a commensurate 4×4 superstructure with a lattice constant of 9.96 Å.

In the line of known C_{60} monolayer systems, C_{60}/*h*-BN/Ni(1 1 1) can be ranged between C_{60} adsorbed on plain metals, where the molecules are spontaneously charged by 1–2 electrons per molecule [3], and insulators or semiconductors, where the molecules remain uncharged [2]. The film structure of C_{60}/*h*-BN/Ni(1 1 1) is illustrated in Fig. 9.8. The electronic properties of the system are illustrated in Fig. 9.9 showing He I_α excited photoemission spectra. The most prominent features of the spectra stem from the C_{60} valence shell, where the highest occupied molecular orbital (HOMO) is marked in

the graph. Comparing spectra at different temperatures, one notices that the C_{60} features are shifted to higher binding energies for the higher temperature, and that the leading edge of the spectrum moves above the Fermi level. This additional intensity arises due to the LUMO that is shifted closer to the Fermi level, thus producing spectral density that reaches into the region of occupied states. A careful analysis of the room-temperature spectra shows that the LUMO is occupied by 0.6 electrons per molecule, on the average.

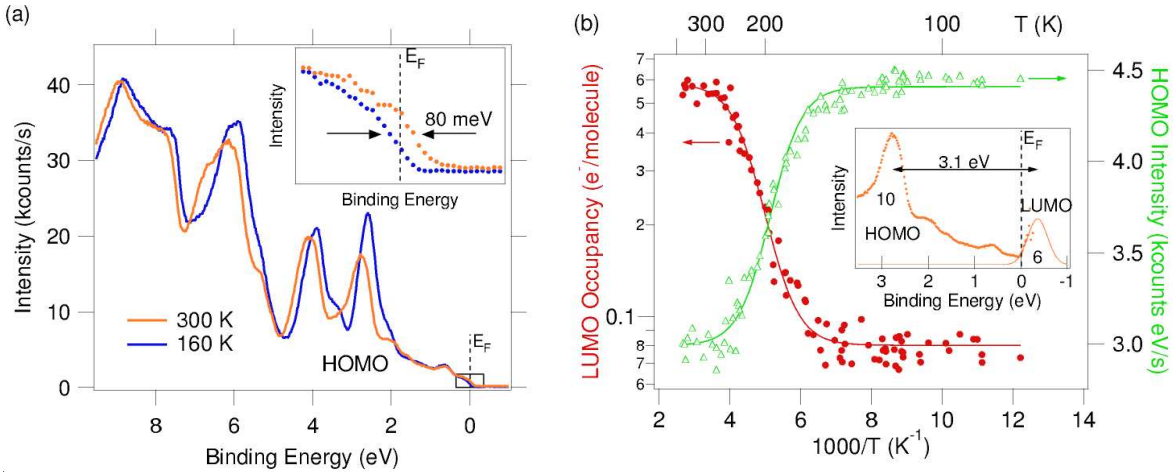

Figure 9.9:
a) Normal emission photoemission spectra ($h\nu = 21.22\,eV$) of the monolayer C_{60}/h-BN/Ni(1 1 1) system at two different temperatures. The inset zooms into the Fermi level region, where a considerable temperature-dependent shift of the leading edge is observed.
b) Calculated LUMO occupancy (red circles), and HOMO peak intensity (green triangles) versus inverse temperature. Both quantities show the same phase transition at around 200 K. The inset displays a measured room temperature spectrum divided by a Fermi-Dirac function, and a fitted Gaussian which indicates the position of the LUMO.

The temperature dependence of the LUMO occupancy (Fig. 9.9b) shows a sharp transition around 200 K. The shape of the curve, as well as the magnitude of the effect, cannot be accounted for by simple thermal activation. Rather, the transition is connected to a structural phase transition. This is further supported by angle-scanned photoelectron diffraction experiments [4], where the structural phase transition is observed in the HOMO intensity curve shown in Fig. 9.9b. From the HOMO intensity, recorded in normal emission, it is concluded that the structural phase transition induces rocking motion that leads to enhanced charge transfer onto the molecule. The magnitude of the charge transfer is unexpectedly high and poses questions that are addressed in continued experimental and theoretical investigations.

[1] W. Auwärter, *One monolayer of hexagonal boron nitride on Ni(111): an atomically sharp interface*, Dissertation, Universität Zürich (2003).
[2] P. Rudolf, M. S. Golden, P. A. Brühwiler, J. Electron Spectrosc. Relat. Phenom. 100 (1999) 409.
[3] C. Cepek, M. Sancrotti, T. Greber, J. Osterwalder, Surf. Sci. 454-456 (2000) 467–471.
[4] M. Muntwiler, *Nanostructured magnetic interfaces: Case studies and new experiment control software*, Dissertation, Universität Zürich (2004).

9.9 Direct determination of the absolute conformation of tartaric acid on Cu(110)

in collaboration with: R. Fasel and K.-H. Ernst, Swiss Federal Lab. for Materials Testing and Research (EMPA), Überlandstr. 129, 8600 Dübendorf, and C. Quitmann, Swiss Light Source, Paul-Scherrer Institut, 5232 Villigen

The interaction between molecules and solid surfaces can cause significant changes of the molecular shape. While in most cases the topological structure like the chirality remains intact, the conformation may change significantly and result in modified functionality of the molecular building blocks [1]. Such structural changes involve torsions of molecular bonds which are driven by the subtle energy balance between bonding to preferred substrate sites and stress induced strain and shear of the softest intramolecular bonds. For the example of Pasteur′s tartaric acid ($C_4H_6O_6$) adsorbed on Cu(110) we determined the absolute chirality and the conformation of the two bitartrate ($C_4H_4O_6$) enantiomers directly [2]. This is obtained by angle-scanned x-ray photoelectron diffraction (XPD) which measures the angles of molecular bonds with high accuracy. The experiment relies on an advanced synchrotron radiation source where a high signal-to-background ratio allows the structure determination of low density and low Z molecules in dilute adsorbate systems.

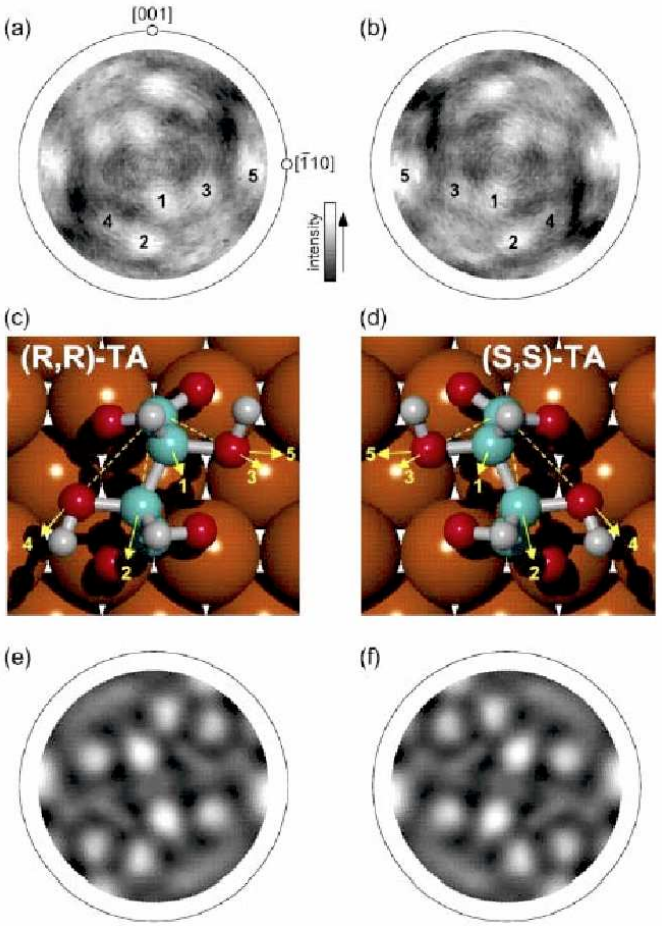

Figure 9.10:
a), b): Experimental C 1s XPD patterns from the (R,R)- and (S,S)-bitartrate adsorbed on Cu(110), respectively.
c), d): Molecular conformations from the geometrical evaluation of the positions of the prominent forward-focusing maxima labeled 1-5 in a) and b). As indicated by the arrows, each peak can be associated to photoelectron emission from one of the C-atoms and forward-focusing by a particular O or C atom.
e), f): Best-fit single-scattering cluster calculations for the (R,R)- and (S,S)-isomers, respectively. The simulations for the optimized molecular conformations accurately reproduce the experimental XPD patterns. From [2].

Figure 9.10 shows the experimental C 1s XPD patterns from the (R,R)- and (S,S)- bitartrate enantiomers adsorbed on the Cu(110) surface [2]. Ten prominent intensity maxima are observed in the patterns, and it is obvious that the patterns from the two enantiomers are mirror images with respect

to each other. Due to the fact that strong intensity maxima correspond to emitter-scatterer directions and that the emitters were selected to be the carbon atoms, the conformation of the carbon backbone and the positions of the hydroxyl-groups relative to the carbon-skeleton are easily determined from the XPD patterns by applying geometrical arguments. In addition to the absolute conformation that results from this straightforward geometrical triangulation, detailed structural parameters can be determined by comparing the experimental XPD pattern to those obtained via calculations, systematically optimizing the structural parameters. The conformation of the (R,R)- bitartrate enantiomer on Cu(110) as predicted from density functional theory (DFT) calculations that did not consider substrate reconstruction [3] is qualitatively similar to the one determined here, but with significantly smaller angular distortions.

[1] S.M. Barlow and R. Raval, Surface Sci. Rep. **50**, 201 (2003).
[2] R. Fasel, J. Wider, C. Quitmann, K.-H. Ernst and T. Greber, Angew. Chem. Int. Edit. (in press).
[3] L. A. M. M. Barbosa, P. Sautet, J. Am. Chem. Soc. **123**, 6639 (2001).

9.10 Time-resolved electron diffraction: space-charge dynamics as tool for characterization

The experimental setup for realizing a low-energy electron diffraction (LEED) experiment with electron pulses of a few picoseconds duration has been completed. First trial experiments on Ge(111) and Ag(111) failed, mainly due to difficulties in finding spatial and temporal overlap of electron and pump light pulses. To overcome this problem, and in order to characterize the electron pulses, a relatively simple electron and light pulse correlation experiment was developed. The setup is depicted in Fig. 9.11. The pulsed electron beam is aimed through a pinhole of 300 μm in diameter drilled into

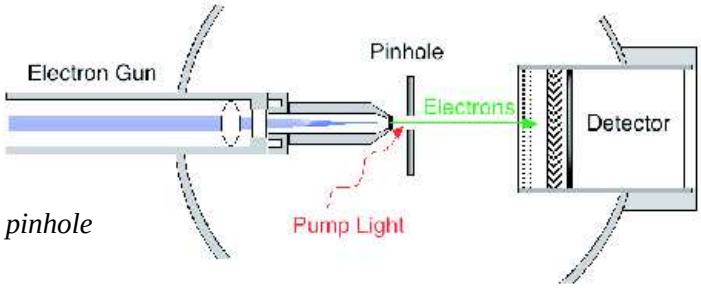

Figure 9.11: *Space-charge experiment: Experimental setup with electron gun, pinhole plate and detector.*

an aluminium plate (thickness 1 mm). Behind the pinhole, electrons are detected by a position sensitive resistive-anode detector with microchannelplate amplifier. Energy filtering is achieved by means of a single copper grid with negative bias voltage in front of the detector. The infrared pump beam (800 nm, fluence on the sample about 10 mJ/cm^2 at 250 kHz repetition rate) is focused into the pinhole creating space charge by the photoelectric effect. Photoelectron spectra, recorded with the same light source from an aluminium plate, showed a broad energy distribution due to multiphoton absorption, with a maximum kinetic energy of roughly 65 eV. The repulsive space charge potential felt by the electrons from the gun produces a negative lens decreasing the transmission through the pinhole. By recording the number of electrons passing through the pinhole as function of delay time between the pump pulse and the electron probe pulse, the temporal evolution of the space charge potential is measured, broadened by the finite time spread of the probing electron pulse. In order to minimize signal fluctuations due to instabilities of the laser, the pump light is chopped with a frequency of roughly 1 Hz. The signal measured with pump light is normalized by the signal without pump light. The experiments were carried out using two different electron guns, one designed for high time resolution

at low energies [1], the second one being a high-energy gun [2]. The guns are referred to hereafter as LEED–gun and MEED–gun, respectively. Electrons are produced in both guns by two-photon-photoemission with the second harmonic of the fundamental wavelength of the Ti:sapphire laser. In order to minimize the temporal broadening of the pulses in the rather long (30 cm) MEED–gun the lens potentials were optimized by means of ray-tracing calculations [3]. Briefly, immediately after emission from the cathode, the electrons are accelerated to energies of the order of 3 keV, and decelerated to their final kinetic energies at the end of the gun. By this optimization, the total flight time of the electrons from the cathode to the sample could be reduced from 48 ns to about 27 ns. The temporal broadening which should scale accordingly was estimated *a priori* to be of the order of 150 to 200 ps.

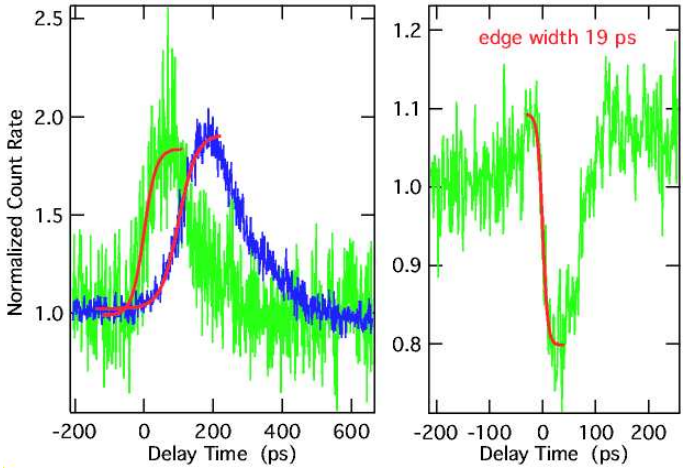

Figure 9.12: *Space-charge experiment: Left: Comparison of the results obtained for the two electron guns used (LEED–gun: green curve, MEED–gun: blue curve). The curves have been scaled to the same height and offset for the sake of clarity; the red lines denote fits to the leading edge.*
Right: Best result obtained so far using the LEED–gun, the edge has a total width of 19 ps.
All curves have been recorded using electron pulses of 200 eV energy.

Indeed, first measurements revealed sizeable effects as shown in Fig. 9.12. The transmission of 200 eV electrons shows a steep decrease by about 30% within 19 ps for electron pulses from the LEED–gun, followed by an exponential increase, fitted with a time constant of 54 ps. Edge and decay of the curves were fitted separatly due to the lack of an analytical function describing the temporal evolution of the space-charge potential. It is safe to conclude that the width of the leading edge of the dip represents an upper limit for the temporal spread of the electron pulses. The value of 19 ps is not far from the value of 5 ps which was the initial design goal [1]. It is interesting to note that the largest effects observed correspond to a transient *increase* in transmission through the pinhole, as plotted in Fig. 9.12 for selected measurements with both guns. The time scales of leading edge and exponential decay are larger than in the case of the dip. We obtain 50 to 70 ps for the leading edge with the LEED–gun indicating that the width of the edge is largely determined by the build-up of the space charge. The decay has a time constant of about 120 ps. The time constants obtained with the MEED–gun are comparable, 103 ps for the rise and 140 ps for the decay, consistent with a time-resolution of about 100 ps of the MEED–gun operated at 200 eV. The increase of transmission is likely to be caused by charges close to the border of the pinhole which produce a positive lens that focuses the incoming electron beam and, thereby, increases the transmission. This conjecture was supported by ray-tracing calculations. Furthermore, curves with different shapes like a peak following a dip and vice versa have been observed, but even a qualitative modeling of these complex shapes is beyond the scope of our research. In conclusion, this experiment allows to characterize the temporal and spatial overlap of electron probe and light pump pulses. Furthermore, the width of narrow features sets an upper limit for the temporal broadening of electron pulses. The method represents a simple and powerful tool for future time-resolved electron diffraction experiments.

[1] R. Karrer, H.J. Neff, M. Hengsberger, T. Greber, and J. Osterwalder, Rev. Sci. Instr. **72**, 4404 (2001).

[2] M. Aeschlimann, E. Hull, C.A. Schmuttenmaer, J. Cao,Y. Gao, D.A. Mantell, and H.E. Elsayed-Ali, Proc. SPIE **2521**,103 (1995).

[3] SIMION software package, Idaho NationalEngineering Laboratory, EG&G Idaho Inc., Idaho Falls.